

Calibration-Based Phase Coherence of Incoherent and Quasi-Coherent 160-GHz MIMO Radars

André Dürr¹, *Student Member, IEEE*, Raphael Kramer, Dominik Schwarz¹,

Martin Geiger¹, *Student Member, IEEE*, and

Christian Waldschmidt¹, *Senior Member, IEEE*

Abstract—Imaging radars are usually realized fully coherently. However, the distribution of one common radio frequency signal to all transmit and receive paths requires a high degree of hardware complexity. In order to reduce the hardware effort significantly, a novel phase synchronization method for incoherent and quasi-coherent frequency-modulated continuous-wave (FMCW) imaging radars with individual signal synthesis per channel is presented. The quasi-coherent setup uses one common oscillator for all frequency synthesizers. It is shown that in the case of the quasi-coherent system, only a phase difference between the calibration and the measurement has to be corrected to achieve coherence. In comparison, an incoherent system causes additional time, frequency, and FMCW ramp slope errors due to the different behavior of the oscillators. In order to achieve phase coherence and to correct the error sources, a calibration-based method using a defined signal path as part of the radar system is proposed. The imaging radar used for verification of the theory consists of individual single-channel radar monolithic microwave integrated circuits (MMICs) at 160 GHz; each MMIC fed by an individual frequency synthesizer. As shown by measurements, it is possible to achieve phase coherence for both system approaches and to perform angle estimation.

Index Terms—Coherence, direction-of-arrival (DoA) estimation, imaging radar, millimeter wave radar, multiple-input-multiple-output (MIMO) radar, phase noise, synchronization.

I. INTRODUCTION

IMAGING radar sensors are meanwhile used in a variety of automotive, industrial, medical, and security applications [1]. There is a growing demand for low-cost imaging radar sensors with improved detection performance in terms of range and angular resolution. To realize physically small radars, operating frequencies above 100 GHz are used. For reducing the costs of such systems, imaging radar front ends can be built without the use of high-frequency substrates.

In recent years, a large number of ultracompact single-channel monolithic microwave integrated circuit (MMIC)-based sensors above 100 GHz have been introduced [2]–[7]. In this frequency range, most of the radar MMICs have integrated voltage-controlled oscillators, amplifiers, mixers, couplers, phase-locked loops (PLLs), and antennas.

Manuscript received September 20, 2019; revised December 19, 2019; accepted January 17, 2020. Date of publication April 1, 2020; date of current version July 1, 2020. This work was supported by the Deutsche Forschungsgemeinschaft (DFG), German Research Foundation, under Project 317632307. (*Corresponding author: André Dürr.*)

The authors are with the Institute of Microwave Engineering, Ulm University, 89081 Ulm, Germany (e-mail: andre.duerr@uni-ulm.de).

Color versions of one or more of the figures in this article are available online at <http://ieeexplore.ieee.org>.

Digital Object Identifier 10.1109/TMTT.2020.2971187

In order to perform coherent beamforming, imaging radars require a time, frequency, and phase synchronization between the individual transmit (TX) and receive (RX) signal paths [8]. Thus, imaging radars are usually realized fully coherently, i.e., the frequency-modulated continuous-wave (FMCW) ramp oscillator (RO) signal is derived from a single PLL and afterward distributed to the individual TX and RX channels [9]–[14]. In coherent imaging radar systems, phase and amplitude mismatches between the hardware channels are calibrated once, and no further phase synchronization is required.

However, the distribution of the high-frequency signals on the printed-circuit board (PCB) is lossy and requires a thorough design process and expensive high-frequency substrates. These problems become more severe with increasing frequency. Hence, it is desirable to implement an imaging radar consisting of individual MMICs that have integrated the high-frequency signal synthesis already on-chip.

Phase ambiguities have to be synchronized for coherent beamforming if fractional- N PLLs are applied [15]. In addition, timing offsets and frequency errors have to be corrected if the signal generation is based on incoherent clock sources. It is shown in [16] that phase synchronization between incoherent sensor nodes can be achieved by joint processing of the two bistatic radar responses based on a synthetic beat signal. The phase shift required for phase synchronization can be estimated by the arithmetic mean of the two bistatic target phases in the radar response. The phase estimation requires a sufficiently large signal-to-noise ratio (SNR), which is fulfilled in wireless localization due to a line-of-sight signal path. Since the quality of the estimated phase values is SNR-dependent, the estimated phases in radar applications would be of differing quality and depend on the targets in the radar channel. In [17], coherent processing of incoherent sensor nodes becomes feasible by simultaneously broadcasting another FMCW signal in a lower frequency channel. This method requires a line-of-sight signal path between each sensor node and the master station, an additional frequency band, and an increased hardware effort. The exchange of frequency synchronization pulses to compensate for oscillator-related errors reduces the total number of errors but does not compensate for errors caused by the behavior of the individual PLLs [18].

In this article, a novel calibration-based phase synchronization method using a signal path as part of the imaging radar system is proposed. The reflection at the lens focusing the

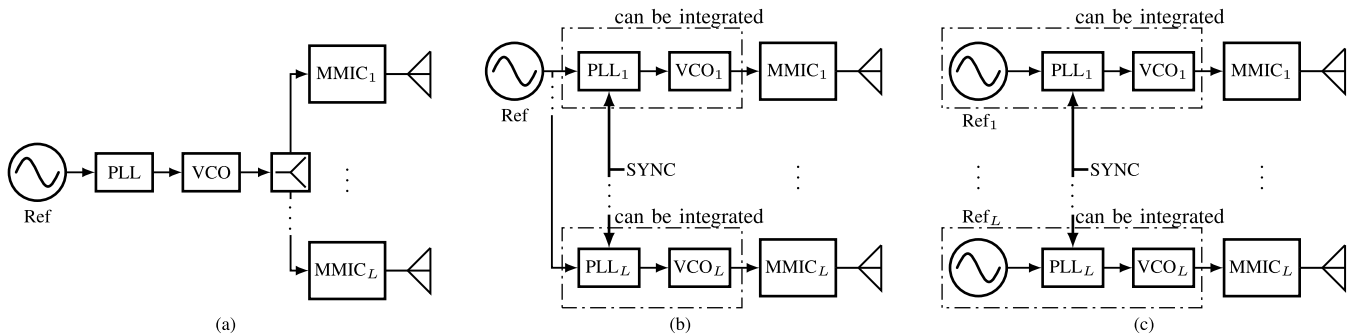


Fig. 1. Block diagrams of different imaging radar system concepts. (a) Coherent system setup using one PLL and an RF signal distribution network. (b) Quasi-coherent signal generation using L individual PLLs with the same reference oscillator. (c) Incoherent signal generation using L individual PLLs with individual reference oscillators.

radiation pattern in the elevation plane may be considered as such a signal path. In contrast to [16], the method presented allows the estimation of a phase correction value using a defined signal path with constant properties and higher amplitude compared with a target in the radar channel. The lens is used as a calibration target to correct phase, frequency, and timing mismatches in a postprocessing step. This results in two new approaches for imaging systems with significantly reduced hardware efforts on PCB. Both system architectures are based on a separate signal generation for each hardware channel. The first approach uses separate PLLs with a common reference oscillator, denoted as a quasi-coherent system setup. The second system approach is based on a typical incoherent signal generation with fully incoherent clock sources. The presented calibration method can be used for both system architectures.

This article is organized as follows. The system concept, the possible error sources, and a corresponding signal model are introduced in Section II. In Section III, the error-correction method is shown for both the quasi-coherent and incoherent system realizations. Finally, the error-correction method is applied to measurement data in Section IV. The reliability of the used error-correction method is proven by direction-of-arrival (DoA) measurements in Section IV. The system performance of the incoherent and quasi-coherent system is compared with a coherent system in Section V.

II. SYSTEM DESCRIPTION

This section provides an overview of the considered system concepts. Subsequently, the possible error sources and a corresponding signal model are given.

A. System Concept

The block diagrams in Fig. 1 show various multichannel imaging radar architectures coming with different hardware efforts on PCB and different related manufacturing costs. The system concepts are technically extendable to any number L of hardware channels. The hardware effort on PCB is reduced from Fig. 1(a)–(c) due to the integration of more hardware components into the MMIC. Typically, imaging radars above 100 GHz are implemented completely coherently, as shown in Fig. 1(a), by distributing a single generated radio frequency (RF) signal between 1 and 100 GHz to

all radar MMICs [8]. In comparison, the radar architectures in Fig. 1(b) and (c) use individual PLLs for the different MMICs and, thus, avoid a distribution of RF signals in the GHz range. By integrating the PLLs and oscillators into the MMIC, the hardware effort on PCB can be reduced significantly. For the quasi-coherent hardware architecture in Fig. 1(b), only an oscillator signal in the MHz range needs to be distributed to the individual radar MMICs, which is feasible with low-cost standard FR4 material. In contrast, no reference signals have to be distributed on the PCB for the incoherent setup. However, the usage of different fractional- N PLLs and different oscillators result in various errors that will be dealt with in Section II-B.

B. Error Sources

The possible error sources between two individual PLLs are described for an incoherent system operation, as shown in Fig. 1(c). The quasi-coherent system shown in Fig. 1(b) is a special case and can be derived from the incoherent signal model.

The RF output f_{RF} of a PLL circuit in the locked state is given by

$$f_{\text{RF}} = \frac{N}{M} f_{\text{Ref}} \quad (1)$$

where N is the feedback divider, M denotes the divider at the input of the phase-frequency detector (PFD), and f_{Ref} is the frequency of the reference oscillator. The error sources are mostly related to variances of the oscillators. The frequency–time diagram and the corresponding error sources of two PLLs with the same settings but different oscillators are summarized in Fig. 2. The frequency output, the increment per clock cycle, and the internal timing counters of the PLL refer to the instantaneous oscillation frequency f_{Ref} of the oscillator at the PFD input. Thus, the following errors between two different incoherent PLLs arise.

- 1) There is a relative drift in time $\Delta t(t)$ as the internal timing counters refer to the reference oscillator.
- 2) A timing offset Δt occurs for the starting point of the ramp as the PFD of each individual PLL locks on the rising/falling edge of its reference oscillator.
- 3) Ramp slope errors arise as the increment per clock cycle depends on the reference oscillator. The ramp slope

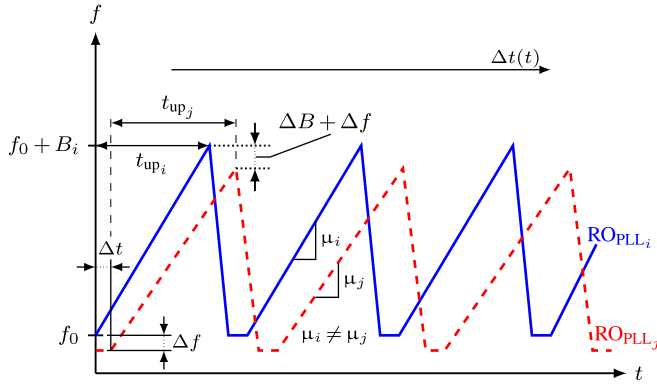


Fig. 2. Frequency-time diagram and related error sources of two incoherent PLLs operating in chirp-sequence frequency modulation.

errors result in a different frequency increment per clock cycle and a different ramp length resulting in both a bandwidth error ΔB and an upchirp time error Δt_{up} . Without loss of generality, PLL_j is now described with deviations with respect to PLL_i. The both mentioned effects provoke a different ramp slope, i.e.,

$$B_i/t_{up_i} = \mu_i \neq \mu_j = (B_i - \Delta B)/(t_{up_i} - \Delta t_{up}).$$

- 4) There is a start frequency offset $\Delta f = f_{0,PLL_i} - f_{0,PLL_j}$ as the ramp start frequencies are related to the individual reference frequencies, as given in (1).
- 5) Phase ambiguities result because the divider value N in fractional- N PLLs toggles between two or more values such that an average divider value for the desired fractional value is achieved. In addition, a lot of divider values are involved in the ramp generation. If the internal register states are not reset or no synchronization signal is provided, different start phases are present at the outputs of the PLLs [15].

Using a common low-cost oscillator for each PLL as in the quasi-coherent system setup shown in Fig. 1(b), the error sources 1)–4) can be avoided. Alternatively, by using ultrahigh quality oscillators, these errors can also be prevented [18].

However, the phase error in 5) remains if different PLLs are used. Thus, no reasonable beamforming can be performed.

C. Signal Model

The mathematical model is given in the following for the incoherent system operation [see Fig. 1(c)] and for a bistatic path $MMIC_i \rightarrow MMIC_j$.

The phase of the transmit signal generated by PLL_i can be described by

$$\begin{aligned} \varphi_{TX_i}(t) &= 2\pi \int_0^t f_0 + \frac{B_i}{t_{up_i}} t_x dt_x + \Phi_i(t) \\ &= 2\pi \left(f_0 t + \frac{B_i}{2t_{up_i}} t^2 \right) + \delta_i + \Phi_i(t) \end{aligned} \quad (2)$$

where $t \in [0, t_{up}]$ denotes the continuous time, δ_i denotes the starting phase of the PLL_i, and $\Phi_i(t)$ denotes the phase noise term.

The local time increments δt_i and δt_j generated by the oscillators Ref_i and Ref_j are given by $\delta t_i = 1/f_{Ref_i}$ and

$\delta t_j = 1/f_{Ref_j}$. Without loss of generality, the transmit signal generated by the PLL_j is affected by a timing offset Δt , a ramp slope error $\mu_j = (B_i - \Delta B)/t_{up_j}$ caused by Δt_{up} and ΔB , and a start frequency offset Δf (see Fig. 2). The relative drift in time $\Delta t(t)$ is caused by the varying time increments δt of the PLLs and occurs if the start time of the ramp block consisting of N_c chirps is just triggered once. Triggering each upchirp individually, the relative drift in time can be neglected (see Section IV-C1). The phase of the transmit signal generated by PLL_j can be described analogously considering deviations with respect to the signal generated in PLL_i and is given by

$$\begin{aligned} \varphi_{TX_j}(t) &= 2\pi \int_0^t (f_0 - \Delta f) + \frac{B_i - \Delta B}{t_{up_j}} (t_x - \Delta t) dt_x + \Phi_j(t) \\ &= 2\pi \left((f_0 - \Delta f) t + \frac{B_i - \Delta B}{2t_{up_j}} t^2 - \frac{B_i - \Delta B}{t_{up_j}} \Delta t t \right) \\ &\quad + \delta_j + \Phi_j(t). \end{aligned} \quad (3)$$

Assuming a channel delay τ_{ji} for the bistatic path, the phase of the received signal at MMIC_j can be described by

$$\begin{aligned} \varphi_{RX_j}(t) &= \varphi_{TX_i}(t - \tau_{ji}) \\ &= 2\pi \left(f_0(t - \tau_{ji}) + \frac{B_i}{2t_{up_i}}(t - \tau_{ji})^2 \right) \\ &\quad + \delta_i + \Phi_i(t - \tau_{ji}). \end{aligned} \quad (4)$$

The phase of the mixed signals after downconversion of the bistatic radar response to baseband can be modeled by

$$\begin{aligned} \Delta\varphi_{ji}(t) &= \varphi_{TX_j}(t) - \varphi_{RX_i}(t) \\ &= 2\pi \left(f_0 t - \Delta f t + \frac{B_i}{2t_{up_j}} t^2 - \frac{\Delta B}{2t_{up_j}} t^2 \right. \\ &\quad \left. - \frac{B_i}{t_{up_j}} \Delta t t + \frac{\Delta B}{t_{up_j}} \Delta t t \right) + \delta_j + \Phi_j(t) \\ &\quad + 2\pi \left(-f_0 t + f_0 \tau_{ji} - \frac{B_i}{2t_{up_i}} t^2 + \frac{B_i}{t_{up_i}} t \tau_{ji} \right. \\ &\quad \left. - \frac{B_i}{2t_{up_i}} \tau_{ji}^2 \right) - \delta_i - \Phi_i(t - \tau_{ji}). \end{aligned} \quad (5)$$

The terms containing $\Delta B \tau_{ji}$, $\Delta B \Delta t$, and τ_{ji}^2 are comparatively small and are, therefore, neglected. Assuming that $t_{up_i} \approx t_{up_j}$, (5) can be simplified to

$$\begin{aligned} \Delta\varphi_{ji}(t) &= 2\pi \left(f_0 \tau_{ji} + \left(\frac{B_i}{t_{up}} (\tau_{ji} - \Delta t) - \Delta f \right) t - \frac{\Delta B}{2t_{up}} t^2 \right) \\ &\quad + \delta_j - \delta_i + \Phi_j(t) - \Phi_i(t - \tau_{ji}). \end{aligned} \quad (6)$$

The instantaneous frequency f_B of the IF beat signal $s_B(t)$ is given by $f_B = 1/2\pi (d/dt \Delta\varphi_{ji}(t))$. According to (6), these errors impact the radar response. The time error Δt and the frequency error Δf result in a falsely estimated target distance. The term $(\Delta B/2t_{up})t^2$ in (6) causes the beat frequency to change within the sweep duration t_{up} , which broadens the target peak within the range spectrum. In addition, the start phase difference $\delta_{ji} = \delta_j - \delta_i$ changes for each radar measurement and has to be calibrated in order to conduct feasible beamforming.

III. ERROR-CORRECTION STEPS

In this section, the calibration setup is given. Afterward, the calibration-based phase and frequency error-correction method are shown for both the quasi-coherent and incoherent system setup using the signal model derived in Section II-C.

A. Calibration Setup

In every radar system, there are differences in the transmission line lengths, RF component variances, and manufacturing uncertainties resulting in phase and amplitude variations among the different TX and RX signal paths. To correct these channel variations, a point-like target, such as a corner reflector, is positioned in the far-field of the antenna array at an azimuth angle $\varphi = 0^\circ$. Then, the radar is rotated around the phase center point of the antenna array in the angular range $-\varphi_{\max} \leq \varphi \leq \varphi_{\max}$, and a radar measurement is conducted for each angular step.

Afterward, a Fourier transform is calculated, and both the phase and the amplitude of the target peak in each virtual channel composed of a TX-RX combination are extracted and stored in a calibration matrix. Evaluating the relative target phases present at the (i, j) -th virtual antenna element with respect to the $(1,1)$ -th virtual antenna element, the relative phase progression is given by [19]

$$\Delta\phi_{ji} = \frac{2\pi}{\lambda} \Delta x_{ji} \sin(\varphi) + \phi_{ji} \quad (7)$$

where i denotes the TX number and j denotes the RX number, $\Delta x_{ji}(\varphi) = x_{ji} - x_{11}$ denotes the virtual antenna distance, and $\phi_{ji} = \phi_j - \phi_i + \delta_{ji}$ denotes the phase offset, which is determined and corrected for beamforming. In the case of coherent radar systems using a single RO, the start phase difference δ_{ji} in (6) can be set to zero as it stems from one PLL. Thus, the phase offset ϕ_{ji} does not change between the measurements and is, therefore, determined once. The start phase difference δ_{ji} between the PLLs can be calibrated with a known and invariable calibration target or signal path within the radar system. For the sake of simplicity, the angle-dependent and constant terms in (7) are neglected for the explanation of the following correction method. The necessary correction steps to establish phase coherence are shown in the following.

B. Quasi-Coherent Correction Method

Using only one common oscillator for all PLLs, the oscillator-related error sources Δt , Δf , and ΔB can be neglected for the quasi-coherent system setup. The phase of the mixed signals derived in (6) simplifies to

$$\Delta\phi_{ji}(t) = 2\pi \left(f_0 \tau_{ji} + \frac{B_i}{t_{\text{up}}} \tau_{ji} t \right) + \delta_{ji}. \quad (8)$$

The phase noise terms in (6) are neglected for the sake of simplicity. Therefore, the start phase difference δ_{ji} must be determined for each measurement cycle, which is possible with a known calibration target. In each measurement, the time-domain beat signal is shifted by the phase $\phi_{ji, \text{cal-target}}$

of the calibration target, and the following correction is applied to the analytic beat signal $s_B^+(t)$:

$$s_{B, \phi\text{-corr}}(t) = s_B^+(t) \exp(-j\phi_{ji, \text{cal-target}}). \quad (9)$$

This operation calibrates the start phase difference δ_{ji} . Note that $\phi_{ji, \text{cal-target}} = \phi_{j, \text{cal-target}} - \phi_{i, \text{cal-target}} + \delta_{ji} \neq \phi_{ji}$ applies because the signal delays between the channels for the defined calibration target within the radar system and a target at an azimuth angle $\varphi = 0^\circ$ are not necessarily equal. Alternatively, the correction can also be applied in the frequency domain.

C. Incoherent Correction Method

The use of different incoherent clock sources for the individual PLLs requires an additional correction of the time error Δt , frequency error Δf , and the FMCW ramp slope error $(\Delta B/2t_{\text{up}})t^2$ in (6). The sequence of the correction steps is as follows.

1) *Ramp Slope Errors*: The ramp slope errors cause that the instantaneous frequency of the bistatic IF spectrum in (6) changes linearly with time. Assuming a known alteration rate $\Delta B/t_{\text{up}}$, the beat frequency signal can be corrected to obtain a beat signal with constant frequency given by

$$s_{B, \text{slope-corr}}(t) = s_B(t) \exp\left(j2\pi \frac{\Delta B}{2t_{\text{up}}} t^2\right). \quad (10)$$

The alteration rate can be exemplarily determined using a short-time Fourier transform of the beat signal. It depends on the modulation and the multiplication factor of the generated RF signal. For radar systems above 100 GHz using large multiplication factors N of the generated RF signals and large bandwidths, the peak broadening is typically in the range of several tens of the range cell size.

2) *Time and Frequency Errors*: Both the time error Δt and the frequency error Δf lead to an incorrectly estimated target distance. As long as the beat signals are within the analog bandwidth, the range spectrum can be shifted in the frequency domain by the operation

$$s_{B, f/t\text{-corr}}(t) = s_{B, \text{slope-corr}}(t) \exp(-j(2\pi \Delta f_{\text{corr}} t)) \quad (11)$$

where Δf_{corr} denotes the frequency shift that is applied to compensate the beat frequency error. This error is determined by evaluating the beat frequency of the known calibration target. Since the starting point of each ramp locks on the rising or falling edge of its reference oscillator, the starting points of both upchirps are affected by jitter. Therefore, the beat frequency of each ramp segment is shifted in the frequency depending on the jitter.

However, jitter of the ramp start time causes a potential image frequency problem. Figure 3 shows the case that the ramp generated at the TX path (—) starts in advance with respect to the ramp generated at the RX path (- - -). This results in a negative beat frequency $f_{B, \text{cal-target}}$ for close targets with a short time-of-travel like a calibration target within the radar system (- - -). The target at larger distance (.....) has a positive beat frequency. Due to the real-valued time-domain signal, the range spectrum is symmetric, and the negative beat frequency peak is also visible in the positive spectral range (—).

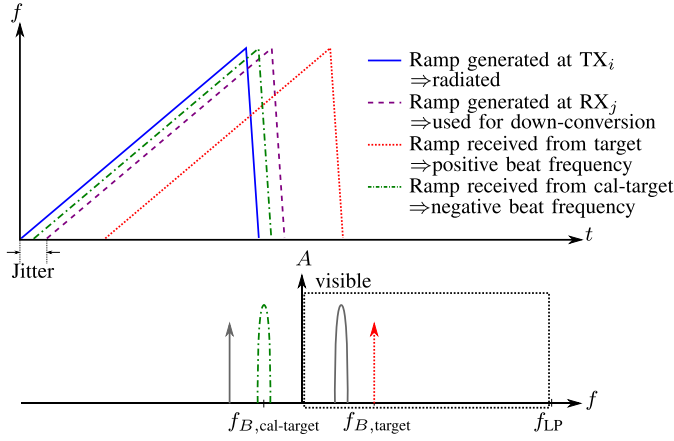


Fig. 3. Frequency–time diagram and corresponding spectrum of the generated ramps of two PLLs. One PLL starts in advance due to jitter in the start time. The solid gray signal components (—) are the image frequencies.

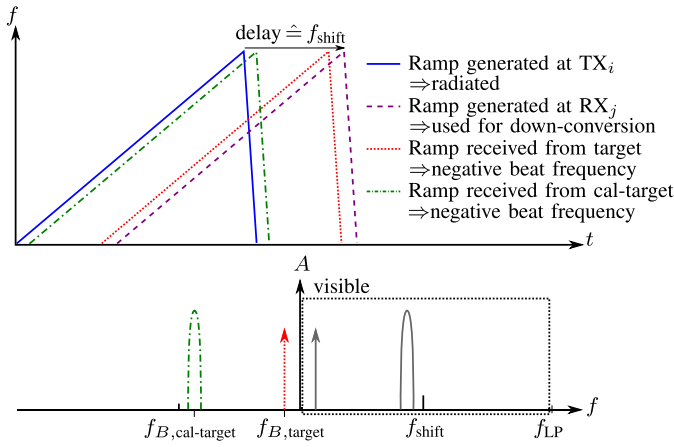


Fig. 4. Frequency–time diagram and corresponding spectrum of the generated ramps of both PLLs. One PLL is intentionally delayed. The solid gray signal components (—) are the image frequencies.

Hence, the distance estimation of the target becomes wrong if it is related to the peak of the close calibration target. This problem can be solved by using an image-rejection mixer [19]. However, this mixer requires twice the number of channels to be sampled, and most single-channel MMICs do not incorporate an image-rejection mixer.

Another possibility is to subdivide the available IF bandwidth in bistatic IF segments as in [20] and to delay PLL_i with respect to PLL_j for a certain number of PFD cycles resulting in a frequency shift $f_{\text{shift}} = f_{LP}/2$ (see Fig. 4). Now, the target peak of the calibration target appears close to f_{shift} ($f_B < f_{\text{shift}}$). All existing targets have either a positive or a negative beat frequency for one bistatic radar response. Thus, the target peaks in the (i, j) -th bistatic channel with positive beat frequency appear to the right of f_{shift} and, in the (i, j) -th bistatic channel with negative beat frequency, appear to the left of f_{shift} as the negative beat frequency is mirrored to the positive frequency domain. Thus, the usable IF bandwidth is reduced by the number of bistatic radar responses, and a larger IF bandwidth is required as in the monostatic radar response.

As each upchirp is affected by an individual jitter, the beat frequency correction in (11) has to be applied to each ramp segment individually.

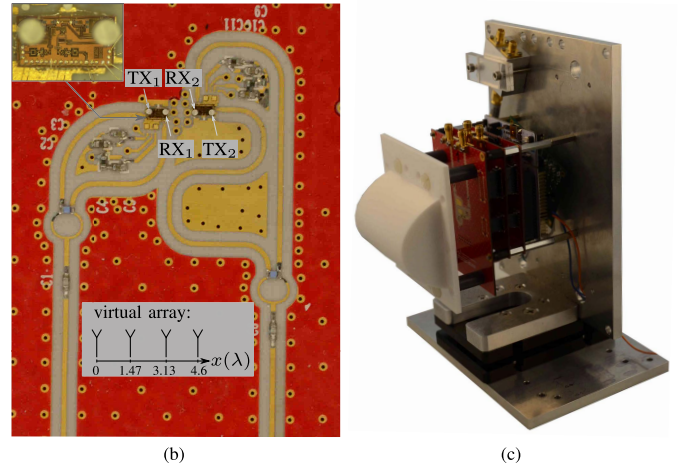
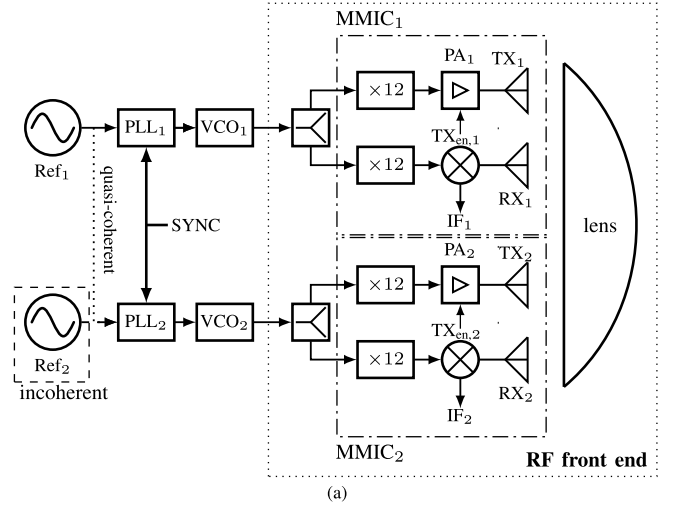


Fig. 5. (a) Block diagram of the realized RF system with the ability to realize a quasi-coherent [see Fig. 1(b)] and incoherent [see Fig. 1(c)] system operation. (b) Photo of the used RF front end PCB. (c) Photo of the used radar setup.

3) *Phase Errors*: After the correction of oscillator-related error sources, the phase errors must be compensated due to the different behavior of the oscillators as in (9). However, in comparison to the quasi-coherent system, the phase correction is applied to each upchirp.

IV. MEASUREMENTS

This section gives an overview of the test hardware used for the verification of the calibration method. Afterward, the theory is proven for both the quasi-coherent and the incoherent error-correction methods.

A. Hardware Demonstrator

The calibration concept is verified using the radar demonstrator, as shown in Fig. 5. The block chart of the hardware demonstrator is given in Fig. 5(a). Figure 5(b) and (c) show the photographs of the RF front end and the radar setup, respectively. The RF front end consists of two radar MMICs and one RF connector for each MMIC. This enables to feed each MMIC with individual RF signals. The MMIC used for the two-channel imaging radar uses separate TX and RX paths

TABLE I
OVERVIEW OF THE RADAR PARAMETERS

Ramp duration t_{up}	250 μs
Ramp repetition time T_r	450 μs
Ramp start frequency f_{start}	12 GHz
Ramp stop frequency f_{stop}	13.67 GHz
RF bandwidth B	20 GHz
Center frequency f_c	153.7 GHz
Number of chirps N_c	512

and a frequency multiplier with factor 12 for the RO signal. The fed-in RO signal is generated from 12 to 13.67 GHz on two separate PLL PCBs and multiplied to the frequency range 144–164 GHz on the MMIC. Afterward, the signal is radiated with on-chip dielectric resonator antennas (DRAs). The system operates with an RF bandwidth of 20 GHz, which results in a range resolution of $\Delta R = 7.5$ mm. The used modulation parameters are summarized in Table I.

Both PLLs can either be operated with the same reference oscillator (quasi-coherent), as shown in Fig. 1(b), or with individual reference oscillators (incoherent), as shown in Fig. 1(c).

The radar MMICs are located below a common dielectric spherical-convex lens made of polytetrafluoroethylene (PTFE). The lens focuses the radiation pattern in the H -Plane, whereas the on-chip antennas are aligned in a row in the E -plane for which the DoA estimation is performed. The lens is used in this work as a defined calibration target. Figure 6 shows the radar response for a monostatic channel (TX₁RX₁) and a bistatic channel (TX₁RX₂) in comparison. The lens represents an extended target in the close proximity of the sensor. Due to the used RF bandwidth of 20 GHz, various independent target peaks become visible. They can be assigned to multiple wave interactions at the lens and are invariant between successive measurements. The outer surface of the lens is identified to have the clearest target reflection in all channels. The lens is static and has a known distance. This information can be used for the time, frequency, and phase synchronizations, as shown in Sections IV-B and IV-C.

The used antenna array consists of two single-channel radar MMICs, each incorporating one TX and one RX antenna with a fixed interelement distance of $d_{\text{TX,RX}} = 1.63$ mm = 0.83λ (at center frequency $f_c = 153.7$ GHz), as shown in Fig. 5(b). The radar system setup uses time-division multiplexing to transmit orthogonal waveforms for multiple-input–multiple-output (MIMO) operation.

B. Verification of the Quasi-Coherent Phase Correction

Independent calibration measurements are conducted for the quasi-coherent system setup [see Fig. 1(b)] with the calibration setup described in Section III-A. After each calibration procedure, the radar is turned off and restarted. The evaluated relative phase progression curves are shown in Fig. 7 for both the defined lens calibration target [see Fig. 7(a) and (b)] and the target at 5 m [see Fig. 7(c) and (d)] for two independent calibration measurements and for a monostatic channel (—) and a bistatic channel (—) in comparison. The relative phase of the target at 5 m behaves according to (7), and it is constant for the lens, which is a defined signal path within the radar

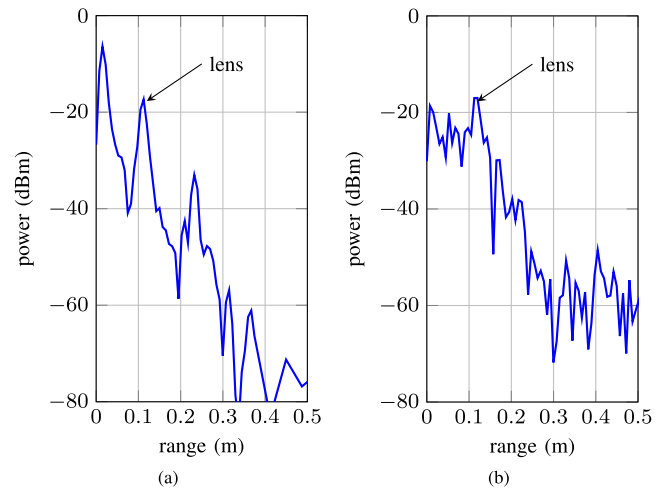


Fig. 6. Measured radar response in the proximity of the radar for (a) monostatic channel (TX₁RX₁) and (b) bistatic channel (TX₁RX₂).

system and, therefore, always appears at $\varphi = 0^\circ$. The constant phase offset ϕ_{ji} is invariant for the monostatic channels (TX₁RX₁, —) and (TX₂RX₂) as the RF signals stem from the same PLL. Figure 7(a) and (b) show that the constant phase offset ϕ_{ji} in (7) changes in the bistatic radar responses for each measurement. This change in constant phase offset is caused in the quasi-coherent system by the varying start phase difference δ_{ji} of the fractional- N PLLs, as described in Section II-B. As shown in Fig. 7(b), the constant phase offset ϕ_{21} for the bistatic channel in (TX₁RX₂, —) has changed by -295° in comparison to the calibration in Fig. 7(a). This change in the constant phase offset is the same for the lens calibration target and the target at 5 m.

The phase ambiguities are mathematically corrected by shifting the time-domain beat signal by the phase $\phi_{ji,\text{cal-target}}$ of the lens calibration target, as in (9). Alternatively, the phase correction can be performed after the Fourier transformation, and target extraction before the beamforming is applied. As shown in Fig. 7, by shifting the relative phase progression curve of the target by the phase of the lens calibration target, almost the same phase progression curves arise for the bistatic channels between successive measurements. This phase correction has to be applied to each measurement block to correct the varying start phase difference δ_{ji} of the PLLs. The same consideration also applies to the other bistatic channel (TX₂RX₁). However, the phase mismatches $\phi_j - \phi_i$ among the hardware channels remain and have to be calibrated once, as for coherent imaging radars.

The calibration method described in Section III-B is applied to five independent measurements for a target whose angle is changed between -10° and 10° in a step size of approximately $\Delta\varphi = 5^\circ$. Figure 8(a) shows, exemplarily, the measured angular spectrum of the target located at $\varphi = 0^\circ$ in comparison to the simulated angular spectrum. It is determined using a Fourier transform of the signals along the virtual antenna positions. The virtual antenna positions are extracted by the measured relative phase progressions [21]. The measurement matches well with the simulated angular spectrum. The estimated angles for the varying target locations

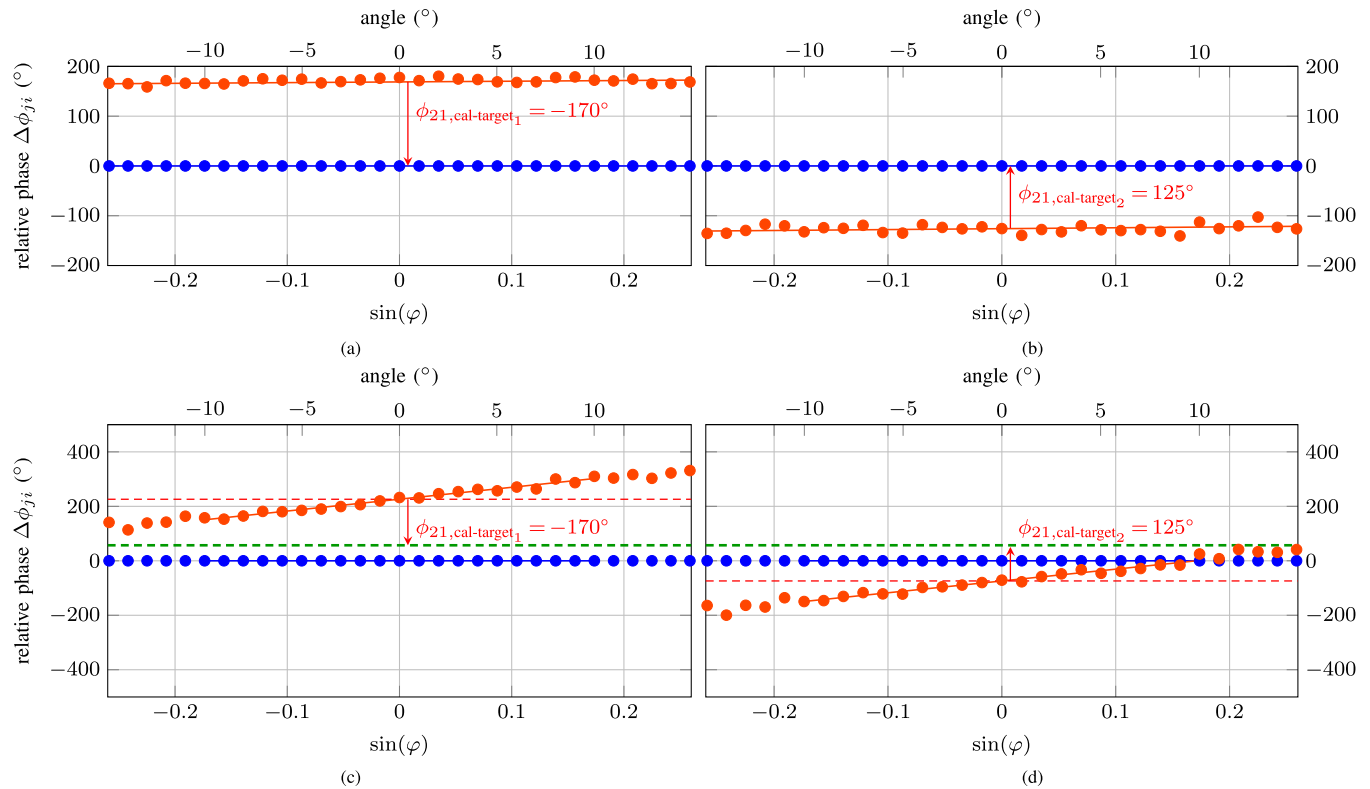


Fig. 7. Measured relative phase progression for two independent calibration procedures (C_1 : calibration 1 and C_2 : calibration 2). (a) Lens calibration target (C_1). (b) Lens calibration target (C_2). (c) Target at 5 m (C_1). (d) Target at 5 m (C_2) for the bistatic channel (TX_1RX_2 , —) and for the monostatic channels (TX_1RX_1 , —).

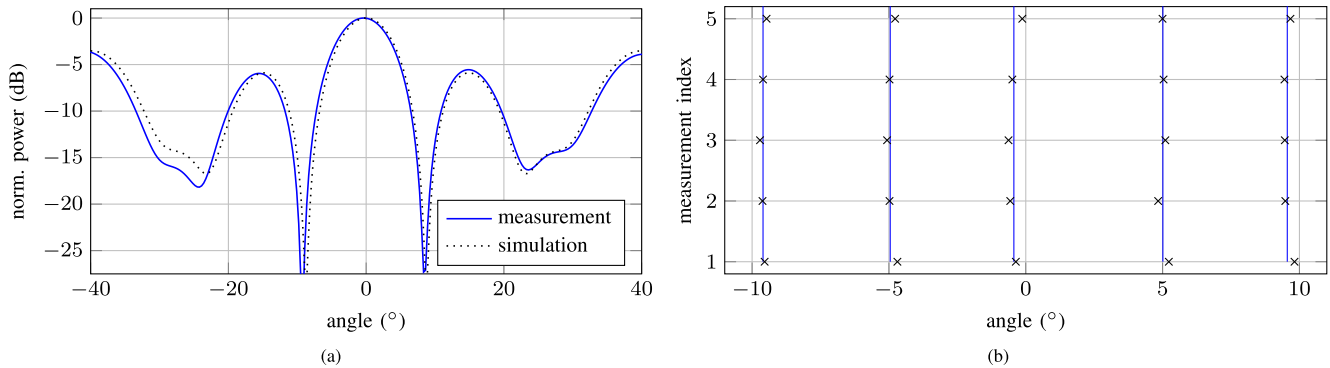


Fig. 8. (a) Measured angular estimation performance for five independent measurements of one target at $\varphi = 0^\circ$ and (b) estimated DoAs for a target approximately located at angles $\varphi \in \{-10^\circ, -5^\circ, 0^\circ, 5^\circ, 10^\circ\}$. The interpolated line (—) shows the mean value of the estimated angles.

are depicted in Fig. 8(b). The measurement results show the DoA always being determined with an overall small standard deviation of 0.13° . This proves that the calibration method is able to correct the phase ambiguities by utilizing the phase of the lens calibration target.

C. Verification of the Incoherent Correction Method

In contrast to the quasi-coherent system setup, which is mainly affected by phase errors, the incoherent system setup, as shown in Fig. 1(c), is also affected by a relative drift $\Delta t(t)$ of the ramp signals in time, a timing offset Δt , ramp slope errors $(B_i - \Delta B)/(t_{up_i} - \Delta t_{up_i})$, and a start frequency offset Δf (see Section II-B).

1) *Relative Drift in Time and Timing Offset*: According to (6), the timing errors lead to a false target distance. When these errors become too large, the IF beat signal lies not within the IF bandwidth of the receiver chain. This timing error is measured with an oscilloscope. Thus, both PLLs are parameterized according to the modulation in Table I. The starting point of the ramp block consisting of 512 upchirps is triggered by a microcontroller. As the local time increments of each PLL stem from two different oscillators, a timing drift, as shown in Fig. 9(a), occurs. The frequency stability of the used 100-MHz oscillators is 25 ppm. The total measured drift in time from upchirp #1 to #512 is approximately $1.6 \mu\text{s}$. This measured drift in time corresponds to a frequency difference

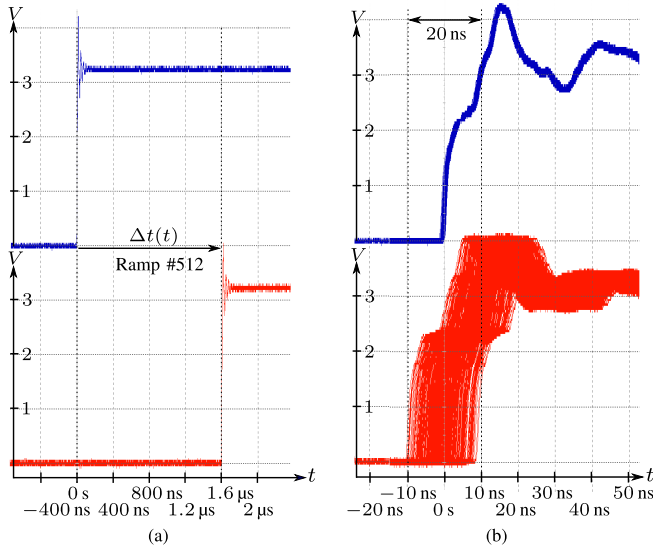


Fig. 9. Ramp clocks for PLL₁ and PLL₂ of the last ramp #512 (a) if the ramp block is triggered once and (b) if each ramp segment is triggered individually. The measurement in (b) shows the ramp clocks of the entire measurement block and is measured using the persistent mode of the oscilloscope.

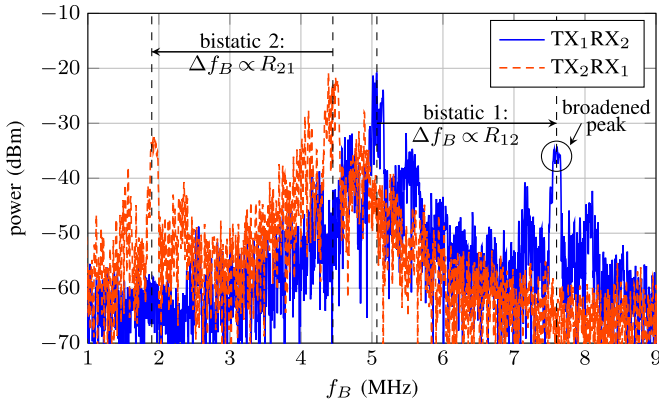


Fig. 10. Measured bistatic target responses for the first ramp.

between both oscillators of approximately 694 Hz and is in accordance with the frequency stability of the used oscillators. A time-of-flight of 1.6 μs represents an IF beat frequency of $f_B \approx 128$ MHz. Therefore, the corresponding beat signals are not within the IF bandwidth of 10 MHz.

Now, each chirp is triggered individually. The measurement results are depicted in Fig. 9(b). The ramp clock of the PLL₂ with respect to PLL₁ is affected by a timing jitter of ± 10 ns, which is one-period length of the frequency of the reference oscillator. It corresponds to a beat frequency of $f_B \approx 800$ kHz now lying within the used IF bandwidth of 10 MHz.

The ramp generated in PLL₁ is delayed by 50 ns, corresponding to the frequency shift f_{shift} . Figure 10 shows the range spectra of both bistatic radar responses of the first ramp. The range spectrum is significantly broadened. Due to the delay of 50 ns of PLL₁ with respect to PLL₂ and additional internal delays, the leakage peaks appear at around 4.3–5.7 MHz. The corresponding bistatic range is measured in relation to the leakage peak.

2) *Ramp Slope Errors*: To correct the ramp slope errors as in (10), the alteration rate has to be estimated. It is determined

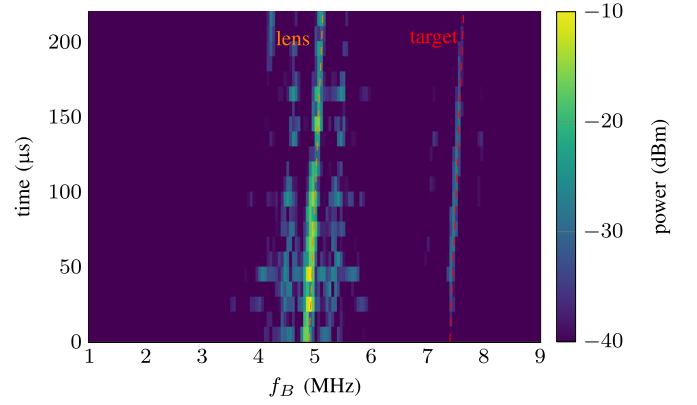


Fig. 11. Measured spectrogram for one bistatic radar response.

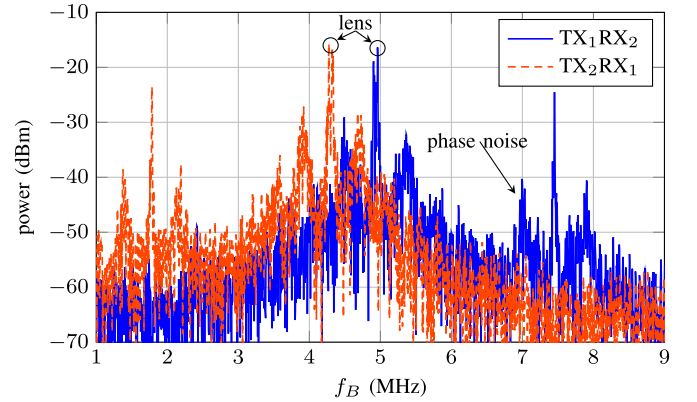


Fig. 12. Corrected measurement data of the bistatic target responses of the first ramp.

by a short-time Fourier transform of the beat signal. The corresponding spectrogram for the bistatic channel TX₁RX₂ is shown in Fig. 11. The upchirp of the length 250 μs is subdivided into 20 segments with the length of 50 μs and an overlapping time of 25 μs . The alteration rate is determined by a least-square fit of the determined target peaks of all segments. Applying the relation in (10) to the time-domain samples, the range spectrum is corrected, as shown in Fig. 12, and the sharp target peaks become visible. The influence of phase noise appears around the targets, which is due to uncorrelated phase noise between the TX signals generated in different PLLs.

3) *Frequency Correction*: The beat frequency of the evaluated and corrected bistatic radar responses in (6) changes for each ramp segment due to the jitter Δt by ± 10 ns in the ramp start time and the start frequency offset Δf (see Fig. 13).

In order to correct the frequency, the target at 5 m and the lens calibration target are determined by a peak search algorithm. Then, the range spectrum is shifted in frequency in such a way that the lens calibration target is located at 5 MHz. Thus, the following correction according to (11) is applied:

$$s_{B,f-\text{corr}}(t) = s_{B,\text{slope-corr}}(t) \exp(-j(2\pi \Delta f_5 \text{ MHz} t))$$

$$\Delta f_5 \text{ MHz} = f_{B,\text{Lens}} - 5 \text{ MHz} \quad (12)$$

where $\Delta f_5 \text{ MHz}$ is the frequency difference between the lens calibration target and 5 MHz. After this step, the timing offset Δt and the start frequency offset Δf are corrected.

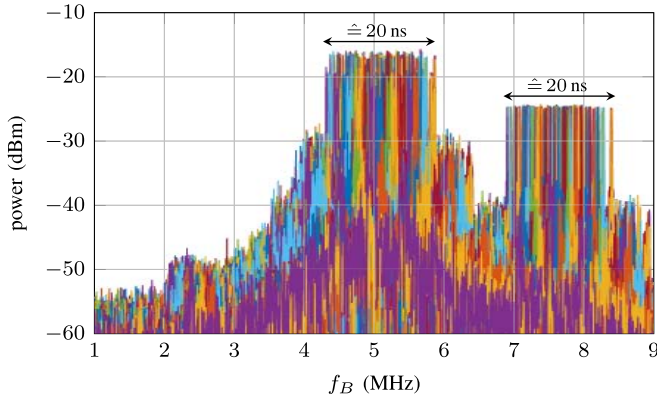


Fig. 13. Superposition of all individual evaluated bistatic radar responses TX₁RX₂ marked with individual colors.

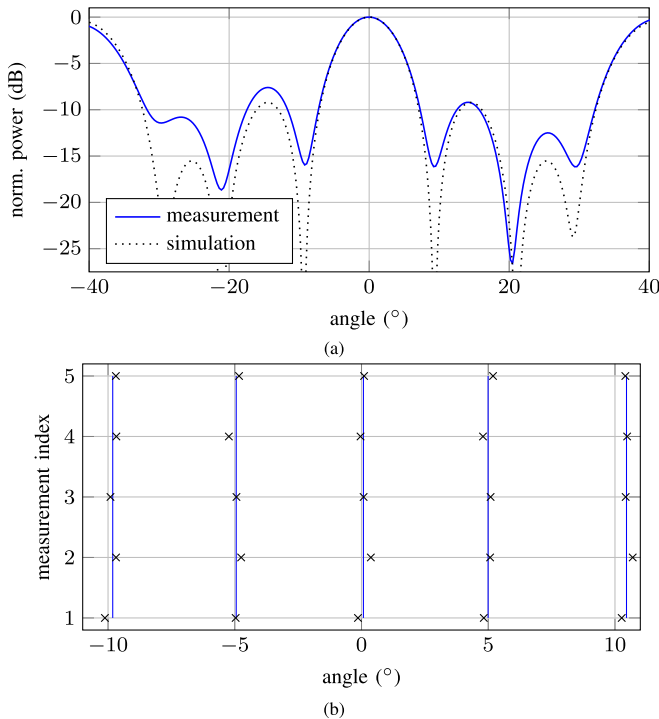


Fig. 14. Measured angular estimation performance for five independent measurements and after correction of timing, slope, frequency, and phase errors of the time-domain signal. (a) Angular spectrum of a target located at $\varphi = 0^\circ$ and (b) estimated DoAs of a target approximately located at angles $\varphi \in \{-10^\circ, -5^\circ, 0^\circ, 5^\circ, 10^\circ\}$. The interpolated line (—) denotes the mean value of the estimated angles.

4) *Phase Correction*: Jitter in the ramp start time also affects the start phase difference δ_{ji} . Hence, phase correction with $\phi_{ji, \text{cal-target}} = \phi_{ji, \text{Lens}}$ in (9) is applied for each ramp segment. After phase correction, the linear relative phase progression as in the quasi-coherent system becomes visible, and the data can be processed coherently (see Fig. 7).

In order to demonstrate the DoA capabilities, measurements are conducted as in the quasi-coherent setup for a target placed at a distance of $R = 5$ m. Figure 14(a) shows the angular spectrum for the target at $\varphi = 0^\circ$ in comparison to the simulated angular spectrum, whereas in Fig. 14(b), the estimated angles of five measurements for various target locations are depicted. As in the quasi-coherent setup, the antenna positions used for

the DoA estimation were determined using the relative phase progressions. The small deviations between simulated and measured angular spectrum result from the fact that the phase has to be estimated without the processing gain of multiple ramps. In contrast to the quasi-coherent setup, the phase and frequency have to be estimated for each ramp segment, instead for the entire measurement block with a processing gain of 256 ramps. In addition, the beat signal is affected by phase noise (see Fig. 12), and the frequency correction steps in Section III are imperfect. However, similar performance in the DoA estimation can be achieved, as shown in Fig. 14(b). The overall standard deviation is 0.18° .

V. COMPARISON OF THE SYSTEM PERFORMANCE

The noise level of the IF signal determines the achievable SNR and the resulting system performance. It is determined by a superposition of thermal noise, quantization noise, and phase noise [8], [22]. In this section, a system performance comparison of the quasi-coherent and the incoherent system after the frequency and phase corrections according to Section III is given. The results are compared with a fully coherent system setup. The beat frequency spectra of all system realizations are shown in Fig. 15. They are calculated with a Fourier transform and evaluated statistically in terms of mean value and standard deviation. The mean value of the beat frequency spectra (—) and the corresponding standard deviation (---) are normalized to the total leakage power.

A. Coherent System

In a coherent system, the same LO is used for the TX and the RX signal paths. Thus, the phase noise of the signals at the downconverting mixer is correlated depending on the time delay τ of the signal in the radar channel [23].

As shown in [8] and [24], the noise level of highly integrated radars with coherent signal generation is determined by thermal noise.

The measurement results for a fully coherent radar operation are shown in Fig. 15(a). The noise level for a single measurement without processing gain coincides with the standard deviation. Since the standard deviation is not increased, there is no increase in the noise level due to uncorrelated phase noise. In addition, the quantization noise level is sufficiently small. Therefore, the noise level is determined by thermal noise.

B. Quasi-Coherent System

For the quasi-coherent system, the noise level is increased due to the residual phase noise around the leakage signal coupling into the adjacent receivers, as shown in Fig. 15(b). The degradation of SNR is caused by the uncorrelated components in both PLLs [8]. However, as shown in [8], the common reference frequency influences the cycling of the PFD resulting in a phase noise suppression of approximately 12 dB at offset frequencies below the loop filter bandwidth of the PLL. The simulated noise level was determined by a convolution of the measured radar response with the measured phase noise of the PLL and demonstrates the improvement of correlation for

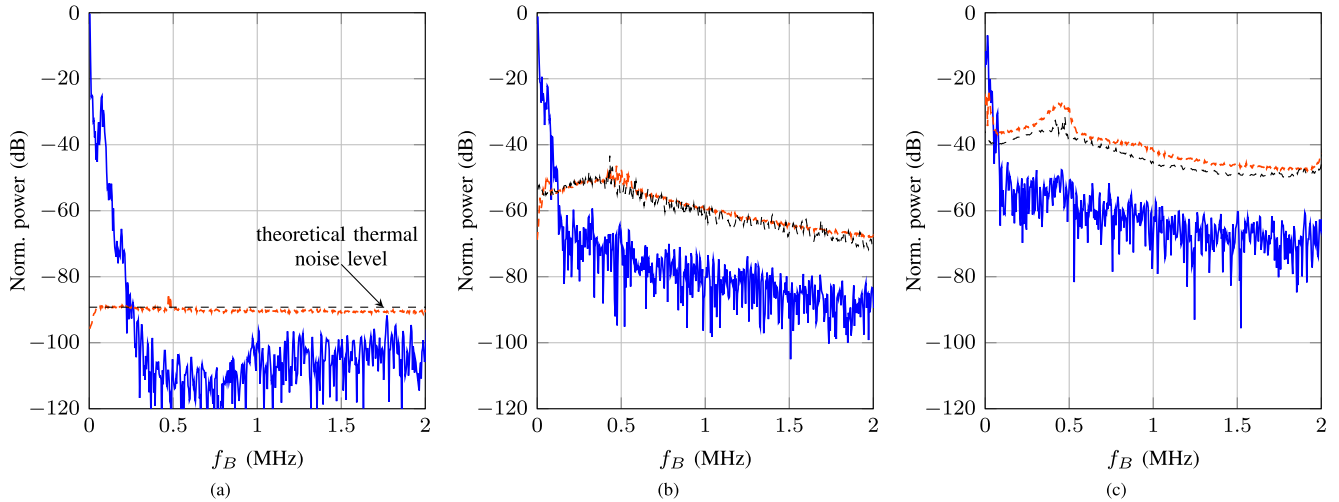


Fig. 15. Measurement results for the bistatic radar response (TX_1RX_2 , —) and the corresponding standard deviation (---) normalized to the total leakage power in comparison to the simulated theoretical noise level (· · ·) for (a) coherent system, (b) quasi-coherent system, and (c) incoherent system.

the quasi-coherent system. The measured phase noise was modified with a phase noise cancellation factor of 12 dB. Measurement and simulation are in good agreement.

C. Incoherent System

For the incoherent system, the noise level is further increased due to uncorrelated phase noise around the leakage signal coupling into the adjacent receivers. For the incoherent system, no correlation is present, and the related phase noise power densities of both PLLs add up in the IF spectrum. Assuming the same phase noise power densities for both PLLs, a deterioration of 3 dB occurs compared with the phase noise of the transmit signal. The deviation of about 3 dB between the measured and simulated noise level can be explained by a loss in amplitude due to the imperfect frequency corrections.

VI. CONCLUSION

In this contribution, a calibration-based phase correction method using a defined signal path within the radar system is proposed. The presented calibration method enables us to realize low-cost imaging radar architectures with significantly reduced hardware effort. The hardware concept is based on the generation of RF signals for the different hardware channels by different PLLs. This allows a higher integration of more hardware components into the MMIC. The correction is applied to both a quasi-coherent architecture using one common oscillator for the two PLLs and an incoherent architecture using independent low-cost oscillators for the two PLLs.

In the case of a quasi-coherent system, only phase ambiguities need to be calibrated for the measurements, while for an incoherent system, ramp start time errors, ramp slope errors, frequency offsets, and phase errors need to be corrected for the sampled IF time-domain signal to achieve coherence. It is verified by radar measurements that all error sources can be corrected for both the quasi-coherent and the incoherent radar operation in a postprocessing step by evaluating the

frequency and the phase of the common dielectric lens calibration target with known properties. DoA estimations employing both system concepts prove the reliability of the used phase synchronization method. The system comparison reveals that for the same power coupling into adjacent receivers, the quasi-coherent system has a better system performance than the incoherent system.

REFERENCES

- [1] R. Lachner, "Industrialization of mmWave SiGe technologies: Status, future requirements and challenges," in *Proc. IEEE 13th Topical Meeting Silicon Monolithic Integr. Circuits RF Syst.*, Jan. 2013, pp. 105–107.
- [2] I. Sarkas, J. Hasch, A. Balteanu, and S. P. Voinigesu, "A fundamental frequency 120-GHz SiGe BiCMOS distance sensor with integrated antenna," *IEEE Trans. Microw. Theory Techn.*, vol. 60, no. 3, pp. 795–812, Mar. 2012.
- [3] M. Jahn, K. Aufinger, and A. Stelzer, "A 140-GHz single-chip transceiver in a SiGe technology," in *Proc. 7th Eur. Microw. Integr. Circuits Conf. (EuMIC)*, Oct. 2012, pp. 361–364.
- [4] T. Jaeschke, C. Bredendiek, and N. Pohl, "A 240 GHz ultra-wideband FMCW radar system with on-chip antennas for high resolution radar imaging," in *IEEE MTT-S Int. Microw. Symp. Dig.*, Jun. 2013, pp. 1–4.
- [5] M. G. Girma, J. Hasch, M. Gonsler, Y. Sun, and T. Zwick, "122 GHz single-chip dual-channel SMD radar sensor with integrated antennas for distance and angle measurements," in *Proc. 11th Eur. Radar Conf.*, Oct. 2014, pp. 1754–1757.
- [6] S. Yuan, A. Strodl, V. Valenta, A. Trasser, and H. Schumacher, "Compact 120–140 GHz radar Tx/Rx sensors with on-chip antenna," in *Proc. IEEE Radio Wireless Symp. (RWS)*, Jan. 2014, pp. 79–81.
- [7] M. Hitzler *et al.*, "Ultracompact 160-GHz FMCW radar MMIC with fully integrated offset synthesizer," *IEEE Trans. Microw. Theory Techn.*, vol. 65, no. 5, pp. 1682–1691, May 2017.
- [8] A. Dürr *et al.*, "High-resolution 160-GHz imaging MIMO radar using MMICs with on-chip frequency synthesizers," *IEEE Trans. Microw. Theory Techn.*, vol. 67, no. 9, pp. 3897–3907, Sep. 2019.
- [9] R. Feger, C. Wagner, S. Schuster, S. Scheibelhofer, H. Jager, and A. Stelzer, "A 77-GHz FMCW MIMO radar based on an SiGe single-chip transceiver," *IEEE Trans. Microw. Theory Techn.*, vol. 57, no. 5, pp. 1020–1035, May 2009.
- [10] A. J. Kirschner, J. Guetlein, S. Bertl, and J. Detlefsen, "A millimetre-wave MIMO radar system for threat detection in patrol or checkpoint scenarios," in *Proc. IET Int. Conf. Radar Syst. (Radar)*, Oct. 2012, pp. 1–6.
- [11] D. Zankl *et al.*, "BLASTDAR—A large radar sensor array system for blast furnace burden surface imaging," *IEEE Sensors J.*, vol. 15, no. 10, pp. 5893–5909, Oct. 2015.

- [12] T. Spreng, S. Yuan, V. Valenta, H. Schumacher, U. Siart, and V. Ziegler, "Wideband 120 GHz to 140 GHz MIMO radar: System design and imaging results," in *Proc. Eur. Microw. Conf. (EuMC)*, Sep. 2015, pp. 430–433.
- [13] D. Bleh *et al.*, "W-band time-domain multiplexing FMCW MIMO radar for far-field 3-D imaging," *IEEE Trans. Microw. Theory Techn.*, vol. 65, no. 9, pp. 3474–3484, Sep. 2017.
- [14] S. Kueppers, H. Cetinkaya, and N. Pohl, "A compact 120 GHz SiGe:C based 2×8 FMCW MIMO radar sensor for robot navigation in low visibility environments," in *Proc. Eur. Radar Conf. (EURAD)*, Oct. 2017, pp. 122–125.
- [15] D. Banerjee, *PLL Performance, Simulation, and Design*, 4th ed. Indianapolis, IN, USA: Dog Ear Publishing, 2006.
- [16] M. Gottinger, F. Kirsch, P. Gulden, and M. Vossiek, "Coherent full-duplex double-sided two-way ranging and velocity measurement between separate incoherent radio units," *IEEE Trans. Microw. Theory Techn.*, vol. 67, no. 5, pp. 2045–2061, May 2019.
- [17] M. Ash, M. Ritchie, K. Chetty, and P. V. Brennan, "A new multistatic FMCW radar architecture by over-the-air deramping," *IEEE Sensors J.*, vol. 15, no. 12, pp. 7045–7053, Dec. 2015.
- [18] H. Breit *et al.*, "Bistatic synchronization and processing of TanDEM-X data," in *Proc. IEEE Int. Geosci. Remote Sens. Symp.*, Jul. 2011, pp. 2424–2427.
- [19] D. Pozar, *Microwave Engineering*, 4th ed. Hoboken, NJ, USA: Wiley, 2012.
- [20] A. Frischen, J. Hasch, and C. Waldschmidt, "A cooperative MIMO radar network using highly integrated FMCW radar sensors," *IEEE Trans. Microw. Theory Techn.*, vol. 65, no. 4, pp. 1355–1366, Apr. 2017.
- [21] A. Dürr *et al.*, "On the calibration of mm-wave MIMO radars using sparse antenna arrays for DoA estimation," in *Proc. 49th Eur. Microw. Conf. (EuMC)*, Oct. 2019, pp. 984–987.
- [22] K. Thurn, R. Ebel, and M. Vossiek, "Noise in homodyne FMCW radar systems and its effects on ranging precision," in *IEEE MTT-S Int. Microw. Symp. Dig.*, Jun. 2013, pp. 1–3.
- [23] M. C. Budge and M. P. Burt, "Range correlation effects in radars," in *Proc. Rec. IEEE Nat. Radar Conf.*, 1993, pp. 212–216.
- [24] M. Hitzler, P. Grüner, L. Boehm, W. Mayer, and C. Waldschmidt, "On monostatic and bistatic system concepts for mm-wave radar MMICs," *IEEE Trans. Microw. Theory Techn.*, vol. 66, no. 9, pp. 4204–4215, Sep. 2018.



André Dürr (Student Member, IEEE) received the M.Sc. degree from Ulm University, Ulm, Germany, in 2017, where he is currently pursuing the Ph.D. degree.

From 2015 to 2016, he was an Intern with the Bosch Research and Technology Center North America, Palo Alto, CA, USA. In 2017, he joined the Institute of Microwave Engineering, Ulm University. His current research interests include novel imaging radar sensor concepts, phase noise mitigation, and performance degradation of noncoherent

multichannel radar systems, and their synchronization, all at millimeter-wave frequencies.

Mr. Dürr was a recipient of the Argus Science Award in 2015, the VDE Award in 2015, and the VDI Award in 2017.



Raphael Kramer received the M.Sc. degree from Ulm University, Ulm, Germany, in 2019.

In 2019, he joined MWI Microwave Ignition AG, Empfingen, Germany, where he is currently working on alternative microwave engine-ignition systems for combustion engines.



Dominik Schwarz received the M.Sc. degree from Ulm University, Ulm, Germany, in 2018, where he is currently pursuing the Ph.D. degree.

From 2011 to 2018, he was a Student Trainee with Hensoldt Sensors, Ulm. In 2018, he joined the Institute of Microwave Engineering, Ulm University. His current research interests include automotive multiple-input–multiple-output (MIMO) radars with a focus on high bandwidths, high channel counts, and novel multilayer printed-circuit board (PCB) structures.

Mr. Schwarz was a recipient of the IfKom Award in 2016.



Martin Geiger (Student Member, IEEE) received the M.Sc. degree from Ulm University, Ulm, Germany, in 2015, where he is currently pursuing the Ph.D. degree.

In 2016, he joined the Institute of Microwave Engineering, Ulm University. His current research interests include novel radar sensor concepts with flexible antennas, dielectric waveguides, and microwave integrated circuits (MMICs) interconnects, all at millimeter-wave frequencies.

Mr. Geiger was a recipient of the Best Student Paper Award of the 2018 International Microwave Symposium.



Christian Waldschmidt (Senior Member, IEEE) received the Dipl.Ing. (M.S.E.E.) and the Dr.Ing. (Ph.D.E.E.) degrees from Universität Karlsruhe (TH), Karlsruhe, Germany, in 2001 and 2004, respectively.

From 2001 to 2004, he was a Research Assistant with the Institut für Höchstfrequenztechnik und Elektronik (IHE), Universität Karlsruhe (TH). Since 2004, he has been with business unit Corporate Research and Chassis Systems, Robert Bosch GmbH, Leonberg, Germany. He was heading different research and development teams in microwave engineering, RF-sensing, and automotive radar. In 2013, he returned to academia. He was appointed as the Director of the Institute of Microwave Engineering, Ulm University, Ulm, Germany, where he is also a Full Professor. He authored or coauthored over 200 scientific publications. He holds more than 20 patents. His research topics focus on radar and RF-sensing, mm-wave and submillimeter-wave engineering, antennas and antenna arrays, and RF and array signal processing.

Dr. Waldschmidt is also a member of the Executive Committee Board of the German MTT/AP Joint Chapter and the German Information Technology Society (ITG). He was a co-recipient of 11 best paper awards since 2014. He has served as the Chair of the IEEE MTT-27 Technical Committee on Wireless Enabled Automotive and Vehicular Applications. He was the two-time TPC Chair and the General Chair of the IEEE MTT International Conference on Microwaves for Intelligent Mobility. Since 2018, he has been serving as an Associate Editor for the IEEE MICROWAVE AND WIRELESS COMPONENTS LETTERS (MWCL). He is also a reviewer for multiple IEEE TRANSACTIONS and many IEEE conferences in the field of microwaves.